

Deterministic realization of collective measurements via photonic quantum walks

Zhibo Hou,^{1,2} Jun-Feng Tang,^{1,2} Jiangwei Shang,^{3,4} Huangjun Zhu,^{5,6,7,8,9,*} Jian Li,^{10,11}
Yuan Yuan,^{1,2} Kang-Da Wu,^{1,2} Guo-Yong Xiang,^{1,2,†} Chuan-Feng Li,^{1,2} and Guang-Can Guo^{1,2}

¹Key Laboratory of Quantum Information, University of Science and Technology of China, CAS, Hefei 230026, P. R. China

²Synergetic Innovation Center of Quantum Information and Quantum Physics,
University of Science and Technology of China, Hefei 230026, P. R. China

³Naturwissenschaftlich-Technische Fakultät, Universität Siegen, Siegen 57068, Germany

⁴Beijing Key Laboratory of Nanophotonics and Ultrafine Optoelectronic Systems,
School of Physics, Beijing Institute of Technology, Beijing 100081, China

⁵Institute for Theoretical Physics, University of Cologne, Cologne 50937, Germany

⁶Department of Physics and Center for Field Theory and Particle Physics, Fudan University, Shanghai 200433, China

⁷Institute for Nanoelectronic Devices and Quantum Computing, Fudan University, Shanghai 200433, China

⁸State Key Laboratory of Surface Physics, Fudan University, Shanghai 200433, China

⁹Collaborative Innovation Center of Advanced Microstructures, Nanjing 210093, China

¹⁰Institute of Signal Processing Transmission, Nanjing University of Posts and Telecommunications, Nanjing 210003, China

¹¹Key Lab of Broadband Wireless Communication and Sensor Network Technology,
Nanjing University of Posts and Telecommunications, Ministry of Education, Nanjing 210003, China

(Dated: March 13, 2022)

Collective measurements on identically prepared quantum systems can extract more information than local measurements, thereby enhancing information-processing efficiency. Although this nonclassical phenomenon has been known for two decades, it has remained a challenging task to demonstrate the advantage of collective measurements in experiments. Here we introduce a general recipe for performing deterministic collective measurements on two identically prepared qubits based on quantum walks. Using photonic quantum walks, we realize experimentally an optimized collective measurement with fidelity 0.9946 without post selection. As an application, we achieve the highest tomographic efficiency in qubit state tomography to date. Our work offers an effective recipe for beating the precision limit of local measurements in quantum state tomography and metrology. In addition, our study opens an avenue for harvesting the power of collective measurements in quantum information processing and for exploring the intriguing physics behind this power.

Quantum measurements are the key for extracting information from quantum systems and for connecting the quantum world with the classical world. Understanding the power and limitation of measurements is of paramount importance not only to foundational studies, but also to many applications, such as quantum tomography, metrology, and communication [1–8]. An intriguing phenomenon predicted by quantum theory is that collective measurements on identically prepared quantum systems may extract more information than local measurements on individual systems, thereby leading to higher tomographic efficiency and precision [9–14]. Recently the significance of collective measurements for multiparameter quantum metrology was also theoretically recognized [15, 16] and experimentally demonstrated with probabilistic Bell measurements as a proof of principle [16]. This nonclassical phenomenon is owing to entanglement in the quantum measurements instead of quantum states. It is closely tied to the phenomenon of “nonlocality without entanglement” [17]. In addition, collective measurements are very useful in numerous other tasks, such as distilling entanglement [18], enhancing nonlocal correlations [19], and detecting quantum change point [20]. However,

demonstrating the advantage of collective measurements in experiments has remained a daunting task. This is because most optimized protocols entail generalized entangling measurements on many identically prepared quantum systems, which are very difficult to realize deterministically.

Here we introduce a general method for performing deterministic collective measurements on two identically prepared qubits based on quantum walks, which extends the method for performing generalized measurements on a single qubit only [21–23]. By devising photonic quantum walks, we realize experimentally a highly efficient collective measurement highlighted in Refs. [11, 13, 14]. As an application, we realize, for the first time, qubit state tomography with deterministic collective measurements. The protocol we implemented is significantly more efficient than local measurements commonly employed in most experiments. Moreover, it can achieve near-optimal performance over all two-copy collective measurements with respect to various figures of merit without using adaptive measurements. Such high efficiency demonstrates the main advantage of collective measurements over separable measurements. Here, we encode the two qubits in the two degrees of freedom of a single photon [24–27], but our method for performing collective measurements can be generalized to two-photon two-qubit states by combining the technique of quantum joining [28] or teleportation [29].

*Electronic address: zhu Huangjun@fudan.edu.cn

†Electronic address: gyxiang@ustc.edu.cn

Results

Optimized collective measurements. In quantum theory, a measurement is usually represented by a positive-operator-valued measure (POVM), which is composed of a set of positive operators that sum up to the identity. In traditional quantum information processing, measurements are performed on individual quantum systems one by one, which often cannot extract information efficiently. Fortunately, quantum theory allows us to perform collective measurements on identically prepared quantum systems in a way that has no classical analog, as illustrated in Fig. 1.

In the case of a qubit, a special two-copy collective POVM was highlighted in Refs. [11, 13, 14], which consists of five POVM elements,

$$E_j = \frac{3}{4}(|\psi_j\rangle\langle\psi_j|)^{\otimes 2}, \quad E_5 = |\Psi_-\rangle\langle\Psi_-|, \quad (1)$$

where $|\Psi_-\rangle = \frac{1}{\sqrt{2}}(|01\rangle - |10\rangle)$ is the singlet, which is maximally entangled, and $|\psi_j\rangle$ for $j = 1, 2, 3, 4$ are qubit states that form a symmetric informationally complete POVM (SIC-POVM), that is, $|\langle\psi_j|\psi_k\rangle|^2 = (2\delta_{jk} + 1)/3$ [30, 31]. Geometrically, the Bloch vectors of the four states $|\psi_j\rangle$ form a regular tetrahedron inside the Bloch sphere. For concreteness, here we choose

$$\begin{aligned} |\psi_1\rangle &= |0\rangle, & |\psi_2\rangle &= \frac{1}{\sqrt{3}}(|0\rangle + \sqrt{2}|1\rangle), \\ |\psi_3\rangle &= \frac{1}{\sqrt{3}}(|0\rangle + e^{\frac{2\pi}{3}i}\sqrt{2}|1\rangle), \\ |\psi_4\rangle &= \frac{1}{\sqrt{3}}(|0\rangle + e^{-\frac{2\pi}{3}i}\sqrt{2}|1\rangle). \end{aligned} \quad (2)$$

The POVM defined by Eqs. (1) and (2) is referred to as the collective SIC-POVM henceforth. If this POVM is performed on the two-copy state $\rho^{\otimes 2}$, then the probability of obtaining outcome j is given by $p_j = \text{tr}(\rho^{\otimes 2} E_j)$.

The collective SIC-POVM is distinguished because it is optimal in extracting information from a pair of identical qubits [9, 11]. It is universally Fisher symmetric in the sense of providing uniform and maximal Fisher information on all parameters that characterize the quantum states of interest [13, 14, 32]. Moreover, it is the unique such POVM with no more than five outcomes. Consequently, the collective SIC-POVM is significantly more efficient than any local measurement in many quantum information processing tasks, including tomography and metrology. Moreover, its high tomographic efficiency is achieved without using adaptive measurements, which is impossible for local measurements.

Realization of the collective SIC-POVM via quantum walks. Recently, discrete quantum walks were proposed as a recipe for implementing general POVMs on a single qubit [21], which have been demonstrated in experiments [22, 23]. In a one-dimensional discrete quantum walk, the system state is characterized by two degrees of freedom $|x, c\rangle$, where $x = \dots, -1, 0, 1, \dots$ denotes the walker position, and $c = 0, 1$ represents the

coin state. The dynamics of each step is described by a unitary transformation of the form $U(t) = TC(t)$, where

$$T = \sum_x |x+1, 0\rangle\langle x, 0| + |x-1, 1\rangle\langle x, 1| \quad (3)$$

is the conditional translation operator, and $C(t) = \sum_x |x\rangle\langle x| \otimes C(x, t)$ with $C(x, t)$ being site-dependent coin operators. A general POVM on a qubit can be realized by engineering the coin operators $C(x, t)$ followed by measuring the walker position after certain steps. However, little is known in the literature on realizing POVMs on higher dimensional systems. Here we propose a general method for extending the capabilities of quantum walks. For concreteness, we illustrate our approach with the collective SIC-POVM.

To realize the collective SIC-POVM using quantum walks, the coin qubit and the walker in positions 1 and -1 are taken as the two-qubit system of interest, while the other positions of the walker act as an ancilla. With this choice, the collective SIC-POVM can be realized with five-step quantum walks, as illustrated in Fig. 1d and discussed in more details in the supplement. Here the non-trivial coin operators $C(x, t)$ are specified in the Methods section. The five detectors E_1 to E_5 marked in the figure correspond to the five POVM elements specified in Eqs. (1) and (2). Moreover, this proposal can be implemented using photonic quantum walks, as illustrated in Fig. 2 (see also Supplementary Fig. S1).

Experimental setup. The experimental setup for realizing the collective SIC-POVM and its application in quantum state tomography is presented in Fig. 2. The setup is composed of two modules designed for two-copy state preparation and collective measurements, respectively.

The two-copy collective measurement module performs the collective SIC-POVM based on quantum walks, as illustrated in Fig. 1d (cf. Supplementary Fig. S1). Here the conditional translation operator T is realized by interferometrically stable beam displacers (BDs) [33–36], which displace the component with horizontal polarization (H) away from the component with vertical polarization (V). The coin operators $C(x, t)$ are realized by suitable combinations of half wave plates (HWP) and quarter wave plates (QWP), with rotation angles specified in the table embedded in Fig. 2.

In the two-copy state-preparation module, we first prepare copy 1 in the path degree of freedom, i.e., the walker qubit encoded in positions 1 and -1 (see the green region I in Fig. 2). A pair of 1-mm-long BBO crystals with optical axes perpendicular to each other, cut for type-I phase-matched spontaneous parametric down-conversion (SPDC) process, is pumped by a 40-mW H-polarized beam at 404 nm. The polarization state of the beam is prepared as $\cos 2\alpha_1|H\rangle + \sin 2\alpha_1|V\rangle$ when the deviation angle of the HWP at 404 nm is set at α_1 . After the SPDC process, a pair of photons with wave length $\lambda = 808$ nm is created in the state of $\sin 2\alpha_1|HH\rangle + \cos 2\alpha_1|VV\rangle$ [37].

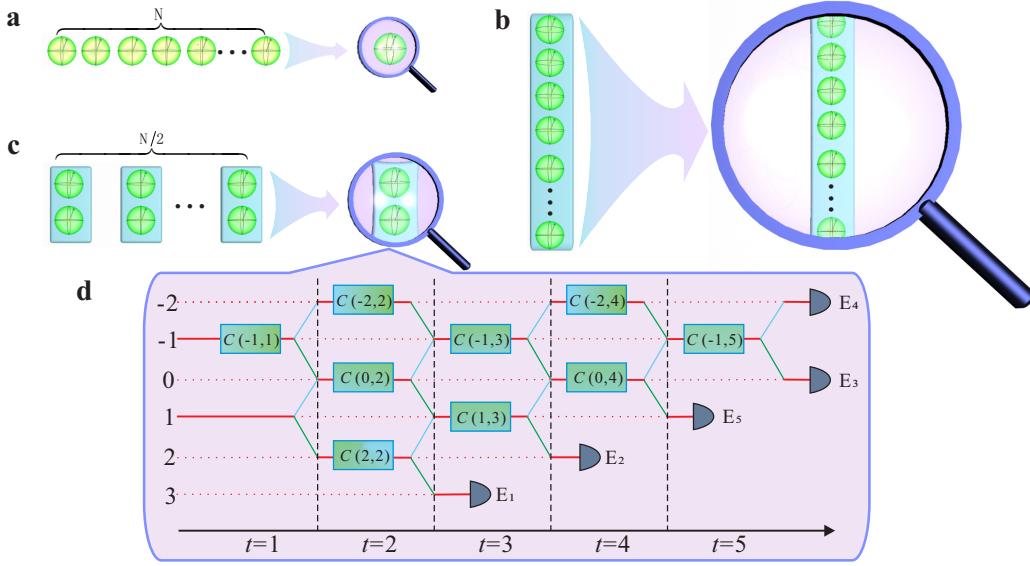


FIG. 1: Individual and collective measurements. **a**: Repeated individual measurements. **b**: Single N -copy collective measurement. **c**: Repeated two-copy collective measurements. **d**: Realization of the collective SIC-POVM defined in Eqs. (1) and (2) using five-step quantum walks. The coin qubit and the walker in positions 1 and -1 are taken as the two-qubit system of interest, while the other positions of the walker act as an ancilla. Site-dependent coin operators $C(x, t)$ are specified in the Methods section. Five detectors E_1 to E_5 correspond to the five outcomes of the collective SIC-POVM.

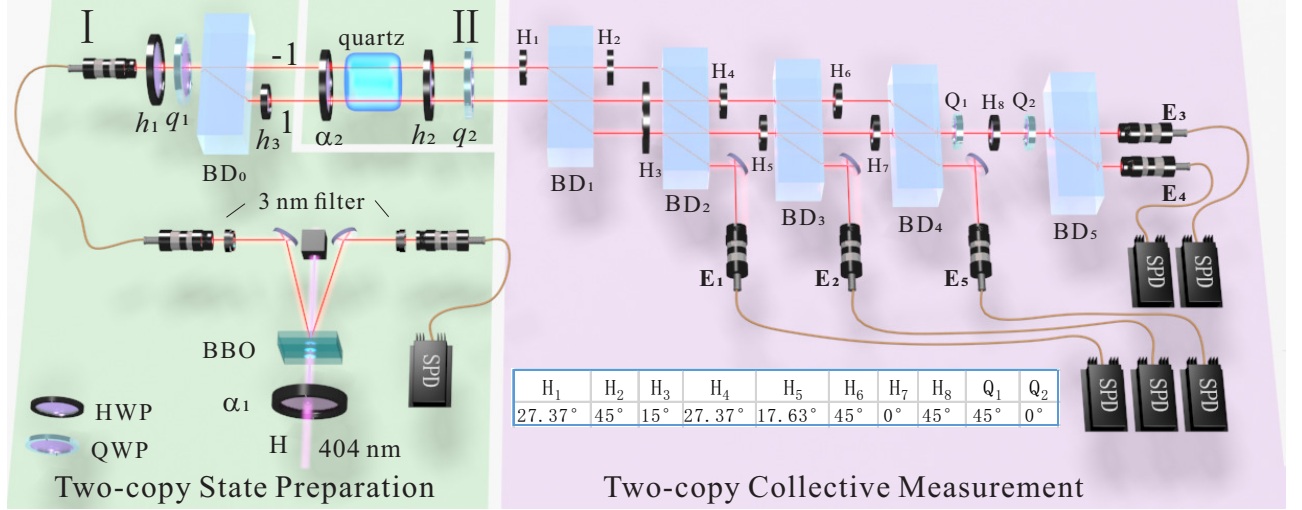


FIG. 2: Experimental setup for realizing the collective SIC-POVM. The setup consists of two modules designed for two-copy state preparation (green) and two-copy collective measurement (purple), respectively. In the two-copy state preparation module, submodule I prepares the first copy (walker qubit) in the path degree of freedom; submodule II prepares the second copy (coin qubit) in the polarization degree of freedom. The two-copy collective-measurement module performs the collective SIC-POVM via photonic quantum walks as illustrated in Fig. 1d. Here beam displacers (BDs) are used to realize the conditional translation operator T . Combinations of half wave plates (HWPs) and quarter wave plates (QWPs) with rotation angles specified in the embedded table are used to realize site-dependent coin operators $C(x, t)$. Five single-photon detectors (SPDs) E_1 to E_5 correspond to the five outcomes of the collective SIC-POVM.

The two photons pass through two interference filters whose FWHM (full width at half maximum) is 3 nm, resulting in a coherence length of 270λ . One photon is detected by a single-photon detector acting as a trigger. After tracing out this photon, the other photon is prepared in the state $\sin^2 2\alpha_1 |H\rangle\langle H| + \cos^2 2\alpha_1 |V\rangle\langle V|$,

whose purity is controlled by α_1 . Two HWPs (not shown in Fig. 2) at the input and output ports of the single-mode fiber are used to maintain the polarization state of the photon. After passing a HWP and a QWP with deviation angles h_1, q_1 , the photon is prepared in the desired state ρ . To encode the polarization state into the

path degree of freedom, BD_0 is used to displace the H-component into path 1, which is 4-mm away from the V-component in path -1; then a HWP with deviation angle $h_3 = 45^\circ$ is placed in path 1. The resulting photon is described by the state $\rho \otimes |V\rangle\langle V|$.

Then we encode the second copy of ρ into the polarization degree of freedom (coin qubit) using two HWPs, a quartz crystal with a decoherence length of 385λ , and a QWP (see the green region II in Fig. 2). The first HWP with rotation angle α_2 and the quartz crystal prepare the polarization state $\sin^2 2\alpha_2 |H\rangle\langle H| + \cos^2 2\alpha_2 |V\rangle\langle V|$ with desired purity. Then the direction of the Bloch vector of the polarization state is adjusted by a HWP and a QWP with deviation angles h_2 and q_2 . In this way, we can prepare the desired two-copy state $\rho \otimes \rho$, the first copy of which is encoded in the path degree of freedom, while the second one in the polarization degree of freedom.

The two-copy state-preparation module described above is capable of preparing any two-copy state. Next, the two-copy state $\rho \otimes \rho$ is sent into the two-copy collective-measurement module, which performs the collective SIC-POVM based on quantum walks, as described before. It is worth pointing out that the collective SIC-POVM can also be applied to measure arbitrary two-qubit states, although we focus on two-copy qubit states in this work.

Experimental verification of the collective SIC-POVM. To verify the experimental implementation of the collective SIC-POVM, we took the conventional method of measuring the probability distributions after preparing the input states as normalized POVM elements, i.e., $\hat{E}_i = E_i / \text{tr}(E_i)$ for $i = 1, \dots, 5$. These input states can be prepared by choosing proper rotation angles $\alpha_1, h_1, q_1, h_3, \alpha_2, h_2, q_2$ as specified in the supplement. The measurement probability distributions are shown in Fig. 3, which agree very well with the theoretical prediction.

To accurately characterize the POVM elements that were actually realized, we then performed quantum measurement tomography. Overall, 36 input states, the tensor products of the six eigenstates of three Pauli operators, were prepared and sent to the collective-measurement module, with each setting repeated 35000 times. Then the five POVM elements were estimated from the measurement statistics using the maximum likelihood method developed in Ref. [38]. The fidelities of the five POVM elements estimated are 0.9991 ± 0.0001 , 0.9979 ± 0.0007 , 0.9870 ± 0.0008 , 0.9927 ± 0.0002 and 0.9961 ± 0.0002 , respectively; the overall fidelity of the POVM (cf. the Methods section) is 0.9946 ± 0.0002 . Here the error bars denote the standard deviations of 100 simulations from Poisson statistics. Such high fidelities demonstrate that the collective SIC-POVM was realized with very high quality. Detailed information about the five reconstructed POVM elements can be found in the supplement.

quantum state tomography with the collective

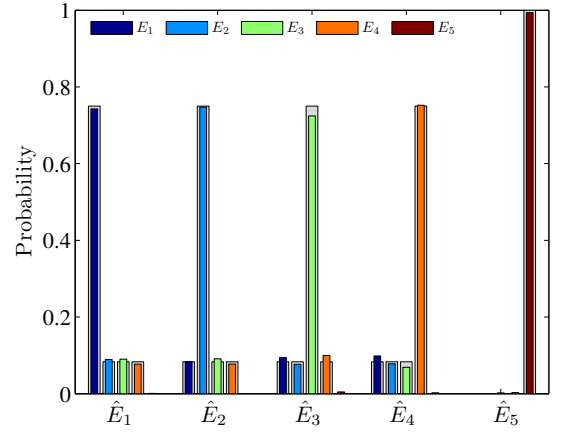


FIG. 3: Experimental verification of the collective SIC-POVM realized. Here each \hat{E}_i for $i = 1, 2, 3, 4, 5$ denotes an input state which corresponds to the POVM element E_i of the collective SIC-POVM after normalization. Each input state is prepared and measured 100000 times. The frequencies of obtaining the five outcomes are plotted using different colors; here the error bars are too small to be visible. For comparison, the probabilities in the ideal scenario are plotted in grey shadow.

SIC-POVM. The experimental realization of the collective SIC-POVM enables us to achieve unprecedented efficiency in quantum state tomography. In this section we demonstrate the tomographic significance of the collective SIC-POVM and the power of collective measurements.

In the first experiment, we investigated the scaling of the mean infidelity $1 - F$ achieved by the collective SIC-POVM with the sample size N (the number of copies of the state available for tomography). Three pure states with Bloch vectors $(0, 0, 1)$, $\frac{1}{\sqrt{2}}(1, 0, 1)$ and $\frac{1}{\sqrt{3}}(1, 1, 1)$ were considered (see the supplement for additional results on mixed states). In each case, the probabilities of obtaining the outcomes of the collective SIC-POVM were estimated from frequencies of repeated measurements, from which we reconstructed the original state using the maximum likelihood method [4]; see the supplement.

The experimental result and simulation result are shown in Fig. 4. Also shown as benchmarks are the simulation results on two popular alternative schemes: one based on mutually unbiased bases (MUB) for a qubit [41–44] and the other based on two-step adaptive measurements proposed in Ref. [45] (cf. Refs. [40, 46, 47]). The experimental result agrees very well with the theoretical predication [14] and numerical simulation. The efficiency of the collective SIC-POVM is almost independent of the input state; the infidelity approximately scales as $O(1/N)$ for all states investigated (cf. Supplementary Table S2). This high efficiency is tied to the fact that the probability of obtaining the outcome E_5 in Eq. (1) is very sensitive to the purity of the input state, so that the purity can be estimated very accurately. By contrast, the scaling behavior is much worse

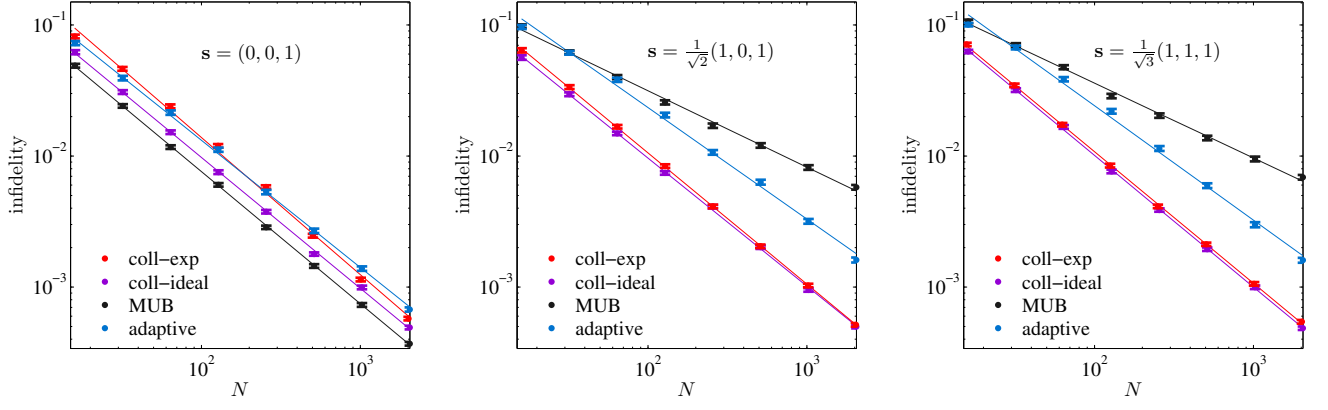


FIG. 4: Scaling of the mean infidelity in quantum state tomography with the collective SIC-POVM (both experiment and simulation). The performances of MUB and two-step adaptive measurements (simulation) are shown for comparison. The three plots correspond to the tomography of three pure states with Bloch vectors \mathbf{s} as specified; N is the sample size, ranging from 16 to 2048. Each data point is the average of 1000 repetitions, and the error bar denotes the standard deviation.

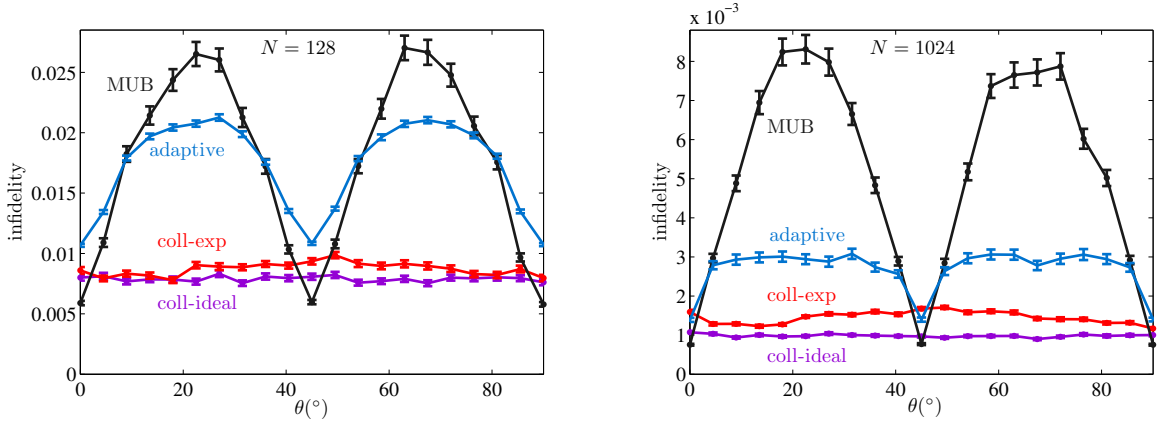


FIG. 5: Mean infidelities achieved by the collective SIC-POVM in estimating pure states of the form $|\psi(\theta)\rangle = \sin \theta|0\rangle + \cos \theta|1\rangle$. The performances of MUB and two-step adaptive measurements (simulation) are shown for comparison. The sample size is $N = 128$ in the left plot and $N = 1024$ in the right plot. Each data point is the average of 1000 repetitions, and the error bar denotes the standard deviation.

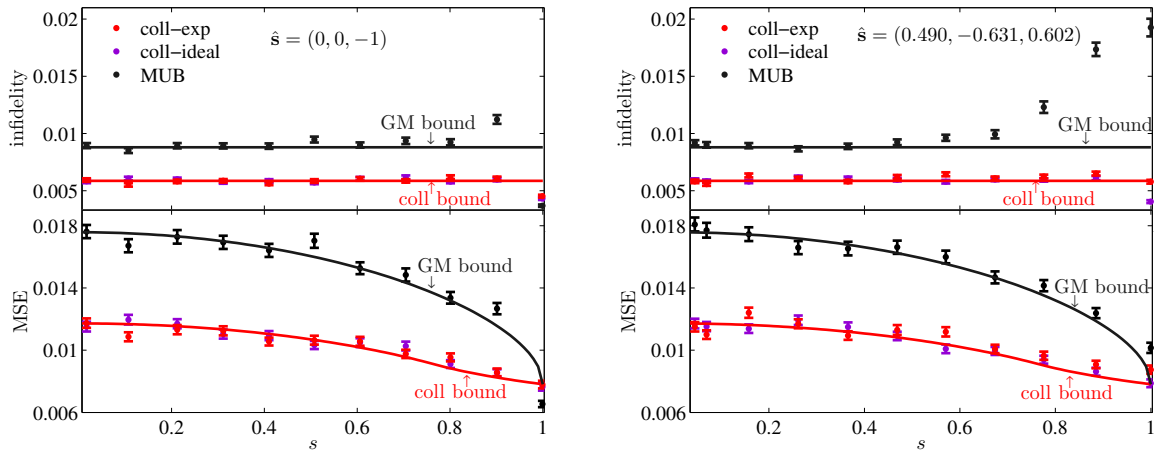


FIG. 6: Performance of the collective SIC-POVM in the tomography of mixed qubit states with respect to the mean infidelity and MSE. Also shown for comparison are the performance of MUB (simulation) as well as the Gill-Massar (GM) bound [13, 39, 40] and a collective (coll) bound [13, 14] (see the Methods section). Here $\hat{\mathbf{s}}$ and s denote the direction and length of the Bloch vector; the sample size is $N = 256$; each data point is the average of 1000 repetitions, and the error bar denotes the standard deviation.

for MUB except when the input state aligns with one of the POVM elements, which corresponds to “known state tomography” [45]. This is because the infidelity is very sensitive to inaccurate estimation of the purity, which is unavoidable for a fixed individual measurement. For a generic pure state, the infidelity achieved by the collective SIC-POVM for $N = 2048$ is approximately twelve (three) times smaller than that achieved by MUB (local adaptive measurements). The advantage of the collective SIC-POVM becomes more significant as the sample size increases.

In the second experiment, we investigated the mean infidelity achieved by the collective SIC-POVM when the input states have the form $|\psi(\theta)\rangle = \sin\theta|0\rangle + \cos\theta|1\rangle$ with θ ranging from 0 to $\pi/2$. Here N is chosen to be 128 (that is, 64 pairs) or 1024 (512 pairs). The result shown in Fig. 5 further demonstrates that the efficiency of the collective SIC-POVM is almost independent of the input state. In addition, the infidelity in the worst scenario is much smaller than that achieved by MUB and local adaptive measurements. As in the first experiment, the advantage of the collective SIC-POVM becomes more significant when N increases.

In the third experiment, we considered two families of mixed states $\rho = \frac{1}{2}(I + \mathbf{s} \cdot \boldsymbol{\sigma})$ with Bloch vectors along $\hat{\mathbf{s}} = (0, 0, -1)$ and $\hat{\mathbf{s}} = (0.490, -0.631, 0.602)$, respectively, and with \mathbf{s} ranging from 0 to 1. The sample size N is chosen to be 256; both the mean infidelity and mean square error (MSE) are considered as figures of merit. The experimental result is shown in Fig. 6. The mean infidelity achieved by the collective SIC-POVM is not only smaller than that by MUB, but also smaller than the Gill-Massar (GM) bound [13, 39, 40], which constrains the performance of any local measurement, even with adaptive choices. Moreover, the mean infidelity approximately saturates a bound derived in Refs. [13, 14], which represents the best performance that can be achieved by two-copy collective measurements; cf. the Methods section. In addition, the collective SIC-POVM is also nearly optimal with respect to the MSE for all states. Remarkably, such high efficiency is achieved without any adaptive measurement.

Discussion

In summary, we introduced a general method for implementing deterministic collective measurements on two identically prepared qubits based on quantum walks. Using photonic quantum walks, we then realized experimentally the collective SIC-POVM with very high quality and thereby achieved unprecedented high efficiency in qubit state tomography. The collective SIC-POVM we realized is significantly more efficient than any local measurement. It improves the scaling of the mean infidelity in the worse scenario from $O(1/\sqrt{N})$ to $O(1/N)$. Moreover, it is nearly optimal over all two-copy collective measurements with respect to various figures of merit, including the mean infidelity and MSE, although no adaptive measurement is required. This high efficiency manifests the

primary advantage of collective measurements over separable measurements.

Our work demonstrated a truly nonclassical phenomenon that is owing to entanglement in quantum measurements instead of quantum states. Moreover, it offers an effective recipe for exceeding the precision limit of local measurements in quantum state tomography. Similar idea can readily be applied to enhance the precision in multiparameter quantum metrology, for instance, in the joint estimation of phase and phase diffusion (cf. Refs. [15, 16]), which deserves further study. More generally, our work opens an avenue for exploring the power of collective measurements in quantum information processing. In the future, it would be desirable to extend our approach to realize multi-copy collective measurements on qubits and systems of higher dimensions.

Methods

Coin operators for realizing the collective SIC-POVM. Here we present the coin operators that appear in Fig. 1d; see Sec. I in the supplement for more details.

$$\begin{aligned} C(-1, 1) &= \frac{1}{\sqrt{3}} \begin{pmatrix} 1 & \sqrt{2} \\ \sqrt{2} & -1 \end{pmatrix}, \quad C(-2, 2) = \begin{pmatrix} 0 & 1 \\ 1 & 0 \end{pmatrix}, \\ C(0, 2) &= \frac{1}{2} \begin{pmatrix} \sqrt{3} & 1 \\ 1 & -\sqrt{3} \end{pmatrix}, \quad C(1, 3) = \frac{1}{\sqrt{3}} \begin{pmatrix} \sqrt{2} & 1 \\ 1 & -\sqrt{2} \end{pmatrix}, \\ C(0, 4) &= \begin{pmatrix} 1 & 0 \\ 0 & -1 \end{pmatrix}, \quad C(-1, 5) = \frac{1}{2} \begin{pmatrix} 1-i & 1+i \\ -1+i & 1+i \end{pmatrix}, \\ C(2, 2) &= C(0, 2), \quad C(-1, 3) = C(-1, 1), \\ C(-2, 4) &= C(-2, 2). \end{aligned} \quad (4)$$

Fidelity between two POVMs. Consider two POVMs $\{E_j\}_{j=1}^M$ and $\{E'_j\}_{j=1}^M$ on a d -dimensional Hilbert space with the same number of elements, where E'_j is the counterpart of E_j (for example, one is the experimental realization of the other). Construct two normalized quantum states as $\sigma = \frac{1}{d} \sum_{j=1}^M E_j \otimes (|j\rangle\langle j|)$ and $\sigma' = \frac{1}{d} \sum_{j=1}^M E'_j \otimes (|j\rangle\langle j|)$, where $|j\rangle$ form an orthonormal basis for an ancilla system. The fidelity between the two POVMs $\{E_j\}_{j=1}^M$ and $\{E'_j\}_{j=1}^M$ is defined as the fidelity between the two states σ and σ' ,

$$F(\sigma, \sigma') := \left(\text{tr} \sqrt{\sqrt{\sigma} \sigma' \sqrt{\sigma}} \right)^2 = \left(\sum_{j=1}^M w_j \sqrt{F_j} \right)^2, \quad (5)$$

where $w_j = \frac{\sqrt{\text{tr}(E_j) \text{tr}(E'_j)}}{d}$, and $F_j = F\left(\frac{E_j}{\text{tr}(E_j)}, \frac{E'_j}{\text{tr}(E'_j)}\right)$ is the fidelity between the two normalized POVM elements $\frac{E_j}{\text{tr}(E_j)}$ and $\frac{E'_j}{\text{tr}(E'_j)}$.

Gill-Massar bounds and collective bounds. In quantum state tomography with individual measurements (including local adaptive measurements), the precision achievable is constrained by the Gill-Massar (GM) bound [13, 39, 40] (see also Ref. [48]). In the case of a

qubit, the GM bound is $\frac{9}{4N}$ when the figure of merit is the mean infidelity (approximately equal to the mean square Bures distance), where N is the sample size (assuming N is not too small). When the figure of merit is the MSE $\mathbb{E} \text{tr}[(\hat{\rho} - \rho)^2]$, the GM bound is $\frac{(2+\sqrt{1-s^2})^2}{2N}$, where s is the length of the Bloch vector of the qubit state.

When collective measurements on two identical qubits are allowed, the precision limit is constrained by a collective bound. According to Eqs. (6.73) and (6.74) in Ref. [13] with $t = 3/2$, the collective bound for the mean infidelity (mean square Bures distance) is $\frac{3}{2N}$ (cf. Ref. [14]), and the bound for the MSE is

$$\begin{cases} \frac{(2+\sqrt{1-s^2})^2}{3N} & \text{if } 0 \leq s \leq \frac{3+4\sqrt{3}}{13}, \\ \frac{s(1+s)(3-s)}{(3s-1)N} & \text{if } \frac{3+4\sqrt{3}}{13} \leq s \leq 1. \end{cases} \quad (6)$$

-
- [1] Helstrom, C. W. *Quantum Detection and Estimation Theory* (Academic Press, New York, 1976).
- [2] Holevo, A. S. *Probabilistic and Statistical Aspects of Quantum Theory* (North-Holland, Amsterdam, 1982).
- [3] Braunstein, S. L. & Caves, C. M. Statistical distance and the geometry of quantum states. *Phys. Rev. Lett.* **72**, 3439–3443 (1994).
- [4] Paris, M. G. A. & Řeháček, J. (eds.) *Quantum State Estimation*, vol. 649 of *Lecture Notes in Physics* (Springer, Berlin, 2004).
- [5] Lvovsky, A. I. & Raymer, M. G. Continuous-variable optical quantum-state tomography. *Rev. Mod. Phys.* **81**, 299 (2009).
- [6] Riedel, M. F. *et al.* Atom-chip-based generation of entanglement for quantum metrology. *Nature* **464**, 1170–1173 (2010).
- [7] Giovannetti, V., Lloyd, S. & Maccone, L. Advances in quantum metrology. *Nature Photonics* **5**, 222 (2011).
- [8] Szczykulska, M., Baumgratz, T. & Datta, A. Multi-parameter quantum metrology. *Advances in Physics: X* **1**, 621–639 (2016).
- [9] Massar, S. & Popescu, S. Optimal extraction of information from finite quantum ensembles. *Phys. Rev. Lett.* **74**, 1259–1263 (1995).
- [10] Gisin, N. & Popescu, S. Spin flips and quantum information for antiparallel spins. *Phys. Rev. Lett.* **83**, 432–435 (1999).
- [11] Vidal, G., Latorre, J. I., Pascual, P. & Tarrach, R. Optimal minimal measurements of mixed states. *Phys. Rev. A* **60**, 126 (1999).
- [12] Bagan, E., Ballester, M. A., Gill, R. D., Muñoz-Tapia, R. & Romero-Isart, O. Separable measurement estimation of density matrices and its fidelity gap with collective protocols. *Phys. Rev. Lett.* **97**, 130501 (2006).
- [13] Zhu, H. *Quantum State Estimation and Symmetric Informationally Complete POMs*. Ph.D. thesis, National University of Singapore (2012). Available at <http://scholarbank.nus.edu.sg/bitstream/10635/35247/1/ZhuHJthesis.pdf>.
- [14] Zhu, H. & Hayashi, M. Universally Fisher-symmetric informationally complete measurements. *Phys. Rev. Lett.* **120**, 030404 (2018).
- [15] Vidrighin, M. D. *et al.* Joint estimation of phase and phase diffusion for quantum metrology. *Nat. Commun.* **5**, 3532 (2014).
- [16] Roccia, E. *et al.* Entangling measurements for multi-parameter estimation with two qubits. *Quantum Sci. Technol.* **3**, 01LT01 (2018).
- [17] Bennett, C. H. *et al.* Quantum nonlocality without entanglement. *Phys. Rev. A* **59**, 1070–1091 (1999).
- [18] Bennett, C. H. *et al.* Purification of noisy entanglement and faithful teleportation via noisy channels. *Phys. Rev. Lett.* **76**, 722–725 (1996).
- [19] Liang, Y.-C. & Doherty, A. C. Better Bell-inequality violation by collective measurements. *Phys. Rev. A* **73**, 052116 (2006).
- [20] Sentís, G., Bagan, E., Calsamiglia, J., Chiribella, G. & Muñoz Tapia, R. Quantum change point. *Phys. Rev. Lett.* **117**, 150502 (2016).
- [21] Kurzyński, P. & Wójcik, A. Quantum walk as a generalized measuring device. *Phys. Rev. Lett.* **110**, 200404 (2013).
- [22] Bian, Z. *et al.* Realization of single-qubit positive-operator-valued measurement via a one-dimensional photonic quantum walk. *Phys. Rev. Lett.* **114**, 203602 (2015).
- [23] Zhao, Y.-Y. *et al.* Experimental realization of generalized qubit measurements based on quantum walks. *Phys. Rev. A* **91**, 042101 (2015).
- [24] Englert, B.-G., Kurtsiefer, C. & Weinfurter, H. Universal unitary gate for single-photon two-qubit states. *Phys. Rev. A* **63**, 032303 (2001).
- [25] Fiorentino, M. & Wong, F. N. C. Deterministic controlled-not gate for single-photon two-qubit quantum logic. *Phys. Rev. Lett.* **93**, 070502 (2004).
- [26] Barreiro, J. T., Wei, T.-C. & Kwiat, P. G. Beating the channel capacity limit for linear photonic superdense coding. *Nature physics* **4**, 282–286 (2008).
- [27] Rubino, G. *et al.* Experimental verification of an indefinite causal order. *Science Advances* **3**, e1602589 (2017).
- [28] Vitelli, C. *et al.* Joining the quantum state of two photons into one. *Nature Photonics* **7**, 521–526 (2013).
- [29] Ahnert, S. E. & Payne, M. C. All possible bipartite positive-operator-value measurements of two-photon polarization states. *Phys. Rev. A* **73**, 022333 (2006).
- [30] Zauner, G. Quantum designs: Foundations of a noncommutative design theory. *Int. J. Quantum Inform.* **09**,

- 445–507 (2011).
- [31] Renes, J. M., Blume-Kohout, R., Scott, A. J. & Caves, C. M. Symmetric informationally complete quantum measurements. *J. Math. Phys.* **45**, 2171 (2004).
 - [32] Li, N., Ferrie, C., Gross, J. A., Kalev, A. & Caves, C. M. Fisher-symmetric informationally complete measurements for pure states. *Phys. Rev. Lett.* **116**, 180402 (2016).
 - [33] O’Brien, J. L., Pryde, G. J., White, A. G., Ralph, T. C. & Branning, D. Demonstration of an all-optical quantum controlled-not gate. *Nature* **426**, 264–267 (2003).
 - [34] Rahimi-Keshari, S. *et al.* Direct characterization of linear-optical networks. *Opt. Express* **21**, 13450–13458 (2013).
 - [35] Rab, A. S. *et al.* Entanglement of photons in their dual wave-particle nature. *Nat. Commun.* **8**, 915 (2017).
 - [36] Shalm, L. K. *et al.* Strong loophole-free test of local realism. *Phys. Rev. Lett.* **115**, 250402 (2015).
 - [37] Kwiat, P. G., Waks, E., White, A. G., Appelbaum, I. & Eberhard, P. H. Ultrabright source of polarization-entangled photons. *Phys. Rev. A* **60**, R773–R776 (1999).
 - [38] Fiurásek, J. Maximum-likelihood estimation of quantum measurement. *Phys. Rev. A* **64**, 024102 (2001).
 - [39] Gill, R. D. & Massar, S. State estimation for large ensembles. *Phys. Rev. A* **61**, 042312 (2000).
 - [40] Hou, Z., Zhu, H., Xiang, G.-Y., Li, C.-F. & Guo, G.-C. Achieving quantum precision limit in adaptive qubit state tomography. *npj Quantum Information* **2**, 16001 (2016).
 - [41] Wootters, W. K. & Fields, B. D. Optimal state-determination by mutually unbiased measurements. *Ann. Phys.* **191**, 363 (1989).
 - [42] Durt, T., Englert, B.-G., Bengtsson, I. & Życzkowski, K. On mutually unbiased bases. *Int. J. Quantum Inform.* **08**, 535 (2010).
 - [43] Adamson, R. B. A. & Steinberg, A. M. Improving quantum state estimation with mutually unbiased bases. *Phys. Rev. Lett.* **105**, 030406 (2010).
 - [44] Zhu, H. Quantum state estimation with informationally overcomplete measurements. *Phys. Rev. A* **90**, 012115 (2014).
 - [45] Mahler, D. H. *et al.* Adaptive quantum state tomography improves accuracy quadratically. *Phys. Rev. Lett.* **111**, 183601 (2013).
 - [46] Kravtsov, K. S. *et al.* Experimental adaptive Bayesian tomography. *Phys. Rev. A* **87**, 062122 (2013).
 - [47] Qi, B. *et al.* Adaptive quantum state tomography via linear regression estimation: Theory and two-qubit experiment. *npj Quantum Information* **3**, 19 (2017).
 - [48] Hayashi, M. A linear programming approach to attainable Cramér-Rao type bounds. In Hirota, O., Holevo, A. S. & Caves, C. M. (eds.) *Quantum Communication, Computing, and Measurement* (Plenum, New York, 1997). Available at arXiv:quant-ph/0102120.
 - [49] Shang, J., Zhang, Z. & Ng, H. K. Superfast maximum-likelihood reconstruction for quantum tomography. *Phys. Rev. A* **95**, 062336 (2017).

Acknowledgements

The work at USTC is supported by the National Natural Science Foundation of China under Grants (Nos. 11574291, 11774334, 61327901 and 11774335), the National Key Research and Development Program of China

(No.2017YFA0304100), Key Research Program of Frontier Sciences, CAS (No.QYZDY-SSW-SLH003), the Fundamental Research Funds for the Central Universities (No.WK2470000026) and China Postdoctoral Science Foundation (Grant No.2016M602012). HZ acknowledges financial support from the Excellence Initiative of the German Federal and State Governments (ZUK 81) and the DFG. JS acknowledges financial support from the ERC (Consolidator Grant 683107/TempoQ), and the DFG.

Author contributions

HZ developed the theoretical approach; GYX supervised the project; ZBH, JFT, JL and GYX designed the experiment and the measurement apparatus for the collective measurement; ZBH built the instruments, performed the experiment and collected the data with assistance from GYX, JFT, YY and KDW; JS developed the maximum likelihood algorithm for state tomography with collective measurements. ZBH, JS, HZ and GYX performed numerical simulations and analysed the experimental data with assistance from CFL and GCG; HZ, ZBH, JS and GYX prepared and wrote the manuscript.

Competing financial interests

The authors declare no competing financial interests.

Deterministic realization of efficient collective measurements via photonic quantum walks: Supplement

I. REALIZATION OF THE COLLECTIVE SIC-POVM VIA QUANTUM WALKS

Recently, quantum walks were proposed as a recipe for implementing general POVMs on a single qubit [21], which have been demonstrated in experiments [22, 23]. In a one-dimensional discrete quantum walk, the system state is characterized by two degrees of freedom $|x, c\rangle$, where $x = \dots, -1, 0, 1, \dots$ denotes the walker position, and $c = 0, 1$ represents the coin state. The dynamics of each step is described by a unitary transformation of the form $U(t) = TC(t)$, where T is the conditional translation operator

$$T = \sum_x |x+1, 0\rangle\langle x, 0| + |x-1, 1\rangle\langle x, 1|, \quad (\text{S1})$$

and $C(t) = \sum_x |x\rangle\langle x| \otimes C(x, t)$ with $C(x, t)$ being site-dependent coin operators. A general POVM on a qubit can be realized by engineering the coin operators $C(x, t)$ followed by measuring the walker position after certain steps. However, little is known in the literature on realizing POVMs on higher dimensional systems based on quantum walks. Here we offer a recipe to extending the capabilities of quantum walks.

For concreteness, we focus on the collective SIC-POVM on a two-qubit system, which is composed of five outcomes,

$$E_j = \frac{3}{4}(|\psi_j\rangle\langle\psi_j|)^{\otimes 2}, \quad E_5 = |\Psi_-\rangle\langle\Psi_-|, \quad (\text{S2})$$

where $|\Psi_-\rangle = \frac{1}{\sqrt{2}}(|\bar{0}\bar{1}\rangle - |\bar{1}\bar{0}\rangle)$ is the singlet, and

$$\begin{aligned} |\psi_1\rangle &= |\bar{0}\rangle, & |\psi_2\rangle &= \frac{1}{\sqrt{3}}(|\bar{0}\rangle + \sqrt{2}|\bar{1}\rangle), \\ |\psi_3\rangle &= \frac{1}{\sqrt{3}}(|\bar{0}\rangle + e^{\frac{2\pi}{3}i}\sqrt{2}|\bar{1}\rangle), & |\psi_4\rangle &= \frac{1}{\sqrt{3}}(|\bar{0}\rangle + e^{-\frac{2\pi}{3}i}\sqrt{2}|\bar{1}\rangle) \end{aligned} \quad (\text{S3})$$

form a symmetric informationally complete POVM (SIC-POVM) on a qubit [30, 31]. Here the “overline” on $\bar{0}, \bar{1}$ is added to distinguish logical quantum states from physical quantum states of the walker and the coin. The Bloch vectors of the four states $|\psi_j\rangle$ for $j = 1, 2, 3, 4$ are given by $\mathbf{r}_1 = (0, 0, 1)$, $\mathbf{r}_2 = (\frac{2\sqrt{2}}{3}, 0, -\frac{1}{3})$, $\mathbf{r}_3 = (-\frac{\sqrt{2}}{3}, \frac{\sqrt{6}}{3}, -\frac{1}{3})$ and $\mathbf{r}_4 = (-\frac{\sqrt{2}}{3}, -\frac{\sqrt{6}}{3}, -\frac{1}{3})$, which form a regular tetrahedron inside the Bloch sphere.

To realize the collective SIC-POVM using quantum walks, the coin qubit and the walker in positions 1 and -1 are taken as the two-qubit system of interest, while the other positions of the walker act as an ancilla. With this choice, the collective SIC-POVM can be realized via five-step quantum walks as illustrated in Fig. 1d in the main text, with nontrivial coin operators given by

$$\begin{aligned} C(-1, 1) &= \frac{1}{\sqrt{3}} \begin{pmatrix} 1 & \sqrt{2} \\ \sqrt{2} & -1 \end{pmatrix}, & C(-2, 2) &= \begin{pmatrix} 0 & 1 \\ 1 & 0 \end{pmatrix}, & C(0, 2) &= \frac{1}{2} \begin{pmatrix} \sqrt{3} & 1 \\ 1 & -\sqrt{3} \end{pmatrix}, \\ C(1, 3) &= \frac{1}{\sqrt{3}} \begin{pmatrix} \sqrt{2} & 1 \\ 1 & -\sqrt{2} \end{pmatrix}, & C(0, 4) &= \begin{pmatrix} 1 & 0 \\ 0 & -1 \end{pmatrix}, & C(-1, 5) &= \frac{1}{2} \begin{pmatrix} 1-i & 1+i \\ -1+i & 1+i \end{pmatrix}, \\ C(2, 2) &= C(0, 2), & C(-1, 3) &= C(-1, 1), & C(-2, 4) &= C(-2, 2). \end{aligned} \quad (\text{S4})$$

To see this, note that a general logical two-qubit pure state

$$|\Psi_0\rangle = a|\bar{0}\bar{0}\rangle + b|\bar{0}\bar{1}\rangle + c|\bar{1}\bar{0}\rangle + d|\bar{1}\bar{1}\rangle, \quad |a|^2 + |b|^2 + |c|^2 + |d|^2 = 1 \quad (\text{S5})$$

can be encoded into the initial state (corresponding to step $t = 0$) of the walker-coin system as

$$|\Psi_0\rangle = a|1, 0\rangle + b|1, 1\rangle + c|-1, 0\rangle + d|-1, 1\rangle. \quad (\text{S6})$$

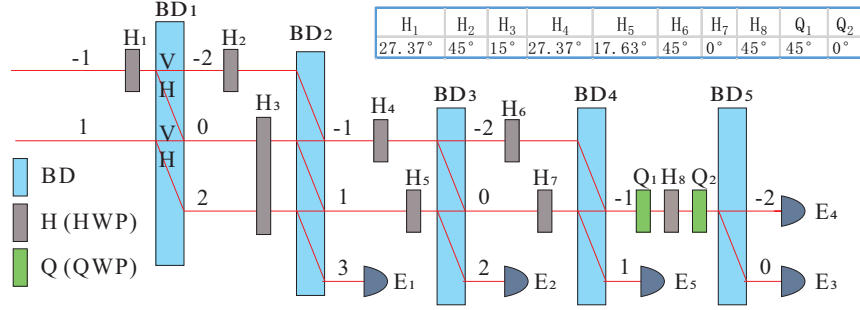


FIG. S1: Realization of the collective SIC-POVM using five-step photonic quantum walks (cf. Fig. 1d and Fig. 2 in the main text). The polarization-encoded coin qubit and the walker in positions 1 and -1 are taken as the two-qubit system of interest, while the other positions of the walker act as an ancilla. Beam displacers (BDs) are used to realize the conditional translation operator T . Combinations of half wave plates (HWP) and quarter wave plates (QWPs) are used to realize site-dependent coin operators $C(x, t)$. Five single-photon detectors (SPDs) E_1 to E_5 correspond to the five outcomes. The collective SIC-POVM is realized by choosing the rotation angles of the HWPs and QWPs according to the table embedded in the figure (identical to the table embedded in Fig. 2).

After step 1, the state $|\Psi_0\rangle$ evolves into

$$|\Psi_1\rangle = TC(t=1)|\Psi_0\rangle = a|2, 0\rangle + b|0, 1\rangle + \left(\sqrt{\frac{1}{3}}c + \sqrt{\frac{2}{3}}d\right)|0, 0\rangle + \left(\sqrt{\frac{2}{3}}c - \sqrt{\frac{1}{3}}d\right)|-2, 1\rangle. \quad (S7)$$

Following a similar procedure, the state after step 5 reads

$$\begin{aligned} |\Psi_5\rangle = & \frac{\sqrt{3}}{2}a|6, 0\rangle + \frac{\sqrt{3}}{6}(a + \sqrt{2}b + \sqrt{2}c + 2d)|4, 0\rangle + \frac{\sqrt{2}}{2}(-b + c)|2, 0\rangle \\ & + \frac{\sqrt{3}}{6}e^{\frac{\pi}{4}i}(a + \sqrt{2}e^{-\frac{2\pi}{3}i}b + \sqrt{2}e^{-\frac{2\pi}{3}i}c + 2e^{-\frac{4\pi}{3}i}d)|0, 0\rangle \\ & + \frac{\sqrt{3}}{6}e^{\frac{\pi}{4}i}(a + \sqrt{2}e^{\frac{2\pi}{3}i}b + \sqrt{2}e^{\frac{2\pi}{3}i}c + 2e^{\frac{4\pi}{3}i}d)|-2, 1\rangle. \end{aligned} \quad (S8)$$

Now measuring the position of the walker realizes the collective SIC-POVM as desired. To verify this claim, note that the probabilities of detecting the walker at positions 6, 4, 2, 0, -2 are respectively given by

$$\begin{aligned} \tilde{p}_6 &= \frac{3}{4}|a|^2 = \frac{3}{4}|\langle\psi_1\psi_1|\Psi_0\rangle|^2 = \langle\Psi_0|E_1|\Psi_0\rangle, \\ \tilde{p}_4 &= \frac{1}{12}|a + \sqrt{2}b + \sqrt{2}c + 2d|^2 = \frac{3}{4}|\langle\psi_2\psi_2|\Psi_0\rangle|^2 = \langle\Psi_0|E_2|\Psi_0\rangle, \\ \tilde{p}_2 &= \frac{1}{2}|-b + c|^2 = |\langle\Psi_-|\Psi_0\rangle|^2 = \langle\Psi_0|E_5|\Psi_0\rangle, \\ \tilde{p}_0 &= \frac{1}{12}|a + \sqrt{2}e^{-\frac{2\pi}{3}i}b + \sqrt{2}e^{-\frac{2\pi}{3}i}c + 2e^{-\frac{4\pi}{3}i}d|^2 = \frac{3}{4}|\langle\psi_3\psi_3|\Psi_0\rangle|^2 = \langle\Psi_0|E_3|\Psi_0\rangle, \\ \tilde{p}_{-2} &= \frac{1}{12}|a + \sqrt{2}e^{\frac{2\pi}{3}i}b + \sqrt{2}e^{\frac{2\pi}{3}i}c + 2e^{\frac{4\pi}{3}i}d|^2 = \frac{3}{4}|\langle\psi_4\psi_4|\Psi_0\rangle|^2 = \langle\Psi_0|E_4|\Psi_0\rangle, \end{aligned} \quad (S9)$$

So the detectors at the five positions 6, 4, 2, 0, -2 correspond to the five POVM elements E_1, E_2, E_5, E_3, E_4 specified in Eqs. (S2) and (S3). Note that a detector at position 6 after step 5 is equivalent to a detector at position 3 after step 2. Similarly, the detector at position 4 (position 2) after step 5 can be placed at position 2 (position 1) after step 3 (step 4) without changing the detection probability. This fact can be utilized to simplify the experimental design, as reflected in Fig. 1 in the main text.

The above proposal can be realized using photonic quantum walks as illustrated in Fig. S1 as well as Fig. 2 in the main text. In this scheme, the conditional translation operator is realized by beam displacers (BDs), which displace the H-component away from the V-component. The coin operators

are realized by suitable combinations of half wave plates (HWPs) and quarter wave plates (QWPs) with rotation angles specified in Fig. S1. Note that a HWP with rotation angle h and a QWP with rotation angle q realize the following unitary transformations

$$U_H(h) = \begin{pmatrix} \cos 2h & \sin 2h \\ \sin 2h & -\cos 2h \end{pmatrix}, \quad U_Q(q) = \frac{1}{\sqrt{2}} e^{\frac{\pi}{4}i} \begin{pmatrix} 1 - i \cos 2q & -i \sin 2q \\ -i \sin 2q & 1 + i \cos 2q \end{pmatrix}. \quad (\text{S10})$$

Based on this equation, it is straightforward to verify that the site-dependent coin operators presented in Eq. (S4) are realized by the wave plates shown in Fig. S1 with rotation angles as specified.

II. STATE PREPARATION

In this section we provide additional details on the preparation of walker-coin two-qubit states considered in the main text. Our discussion is based on the state preparation module illustrated in Fig. 2. Note that the quartz crystal and the HWP corresponding to α_2 are used only in the preparation of mixed states. In general, a walker-coin two-qubit state can be prepared by properly choosing the rotation angles $\alpha_1, \alpha_2, h_1, h_2, h_3, q_1$ and q_2 of the HWPs and QWPs shown in this module. The parameter choices for various states considered in the main text are specified in Table S1. Here $|\pm_z\rangle$, $|\pm_x\rangle$ and $|\pm_y\rangle$ denote the two eigenstates with eigenvalues ± 1 of σ_z , σ_x and σ_y , respectively, with Bloch vectors given by $(0, 0, \pm 1)$, $(\pm 1, 0, 0)$ and $(0, \pm 1, 0)$; these states are used in the measurement tomography of the collective SIC-POVM. \hat{E}_j for $j = 1$ to 5 denote the five normalized POVM elements of the collective SIC-POVM (note that $\hat{E}_1 = |+_z +_z\rangle\langle+_z +_z|$); these states are used in the experimental verification of the collective SIC-POVM. The rest states in the table are studied in quantum state tomography with the collective SIC-POVM. To be specific, $|\psi(\theta)\rangle = \sin \theta |0\rangle + \cos \theta |1\rangle$ is a pure state parametrized by θ ; $\frac{1}{\sqrt{2}}(1, 0, 1)$ and $\frac{1}{\sqrt{3}}(1, 1, 1)$ denote two pure states with Bloch vectors as specified; \mathbf{s}_1 and \mathbf{s}_2 denote quantum states whose Bloch vectors align with $\hat{\mathbf{s}}_1 = (0, 0, -1)$ and $\hat{\mathbf{s}}_2 = (0.490, -0.631, 0.602)$, and with lengths s_1 and s_2 , respectively.

In the preparation of \hat{E}_5 , which is maximally entangled, the QWP corresponding to q_2 is removed, and h_3 is set at 0° . For all other states considered in this work, which are product states, this QWP is present, and h_3 is set at 45° . In the preparation of a product state, α_1, h_1, q_1 are used to control the state of the first qubit (walker), while α_2 (together with the quartz crystal), h_2, q_2 are used to control the state of the second qubit (coin). Specifically, the length of the Bloch-vector of the first qubit is determined by α_1 , while the direction of the Bloch-vector is determined by h_1, q_1 . In the preparation of the second qubit, α_2, h_2, q_2 play similar roles to α_1, h_1, q_1 for the first qubit. The parameters shown in Table S1 apply to the preparation of a two-copy state, of which the walker qubit and the coin qubit are identical. Since the preparation of the two qubit states are independent, product states with different marginals can also be prepared with straightforward modification. For example, the product state $|+_z +_x\rangle$ can be prepared by choosing the following parameters:

$$\alpha_1 = q_1 = 0, \quad h_1 = h_3 = q_2 = 45^\circ, \quad h_2 = -22.5^\circ. \quad (\text{S11})$$

III. QUANTUM MEASUREMENT TOMOGRAPHY OF THE COLLECTIVE SIC-POVM

In this section, we provide more details on the measurement tomography of the collective SIC-POVM realized using photonic quantum walks. To perform measurement tomography, 36 states, the tensor products of the six eigenstates of three Pauli operators, were prepared according to the method described in the previous section and sent to the collective-measurement module. To reduce statistical fluctuation, each state was prepared and measured 35000 times. Then the five POVM elements were estimated from the measurement statistics using the maximum likelihood (ML) method developed in Ref. [38]. The five reconstructed POVM elements are shown in Fig. S2 in comparison with the ideal counterparts. The fidelities of the five POVM elements are 0.9991 ± 0.0001 , 0.9979 ± 0.0007 , 0.9870 ± 0.0008 , 0.9927 ± 0.0002 and 0.9961 ± 0.0002 , respectively; the overall fidelity of the POVM is 0.9946 ± 0.0002 (cf. the Methods section). These results show that the collective SIC-POVM was realized with very high quality.

TABLE S1: Parameter choices in walker-coin two-qubit state preparation. Here $\alpha_1, \alpha_2, h_1, h_2, q_1, q_2$ are the rotation angles of the HWPs and QWPs shown in Fig. 2, and “quartz” denotes the quartz crystal in the same figure. $|\pm_z\rangle, |\pm_x\rangle$ and $|\pm_y\rangle$ denote the two eigenstates with eigenvalues ± 1 of σ_z, σ_x and σ_y ; the parameters in the parentheses apply to the states with eigenvalue -1 . \hat{E}_j for $j = 1$ to 5 denote the five normalized POVM elements of the collective SIC-POVM (note that $\hat{E}_1 = |+_z +_z\rangle\langle+_z +_z|$). $|\psi(\theta)\rangle = \sin\theta|0\rangle + \cos\theta|1\rangle$ is a pure state. $\frac{1}{\sqrt{2}}(1, 0, 1)$ and $\frac{1}{\sqrt{3}}(1, 1, 1)$ denote two pure states with Bloch vectors as specified. \mathbf{s}_1 and \mathbf{s}_2 denote quantum states whose Bloch vectors align with $\hat{\mathbf{s}}_1 = (0, 0, -1)$ and $\hat{\mathbf{s}}_2 = (0.490, -0.631, 0.602)$, and with lengths s_1 and s_2 , respectively; $\alpha(s) = \frac{1}{4} \arccos(s)$. The quartz and the HWP corresponding to α_2 are used only in the preparation of mixed states (in the last two columns of the table). In the preparation of \hat{E}_5 , the QWP corresponding to q_2 is removed.

States	$ \pm_z\rangle$	$ \pm_x\rangle$	$ \pm_y\rangle$	\hat{E}_2	\hat{E}_3	\hat{E}_4	\hat{E}_5	$\frac{1}{\sqrt{2}}(1, 0, 1)$	$\frac{1}{\sqrt{3}}(1, 1, 1)$	$ \psi(\theta)\rangle$	\mathbf{s}_1	\mathbf{s}_2
α_1	0	0	0	0	0	0	0	0	0	0	$\alpha(s_1)$	$\alpha(s_2)$
$h_1(^{\circ})$	45(0)	-22.5(22.5)	-22.5(22.5)	-17.63	0	27.37	22.5	56.25	-24.95	$90 - \frac{\theta}{2}$	0	45
$q_1(^{\circ})$	0	45	0	-35.26	27.37	27.37	45	22.5	22.5	$-\theta$	0	19.57
$h_3(^{\circ})$	45	45	45	45	45	45	0	45	45	45	45	45
$\alpha_2(^{\circ})$	—	—	—	—	—	—	—	—	—	—	$\alpha(s_1)$	$\alpha(s_2)$
quartz	—	—	—	—	—	—	—	—	—	—	0	0
$h_2(^{\circ})$	45(0)	-22.5(22.5)	-22.5(22.5)	-17.63	0	27.37	45	56.25	-24.95	$90 - \frac{\theta}{2}$	0	45
$q_2(^{\circ})$	0	45	0	-35.26	27.37	27.37	—	22.5	22.5	$-\theta$	0	19.57

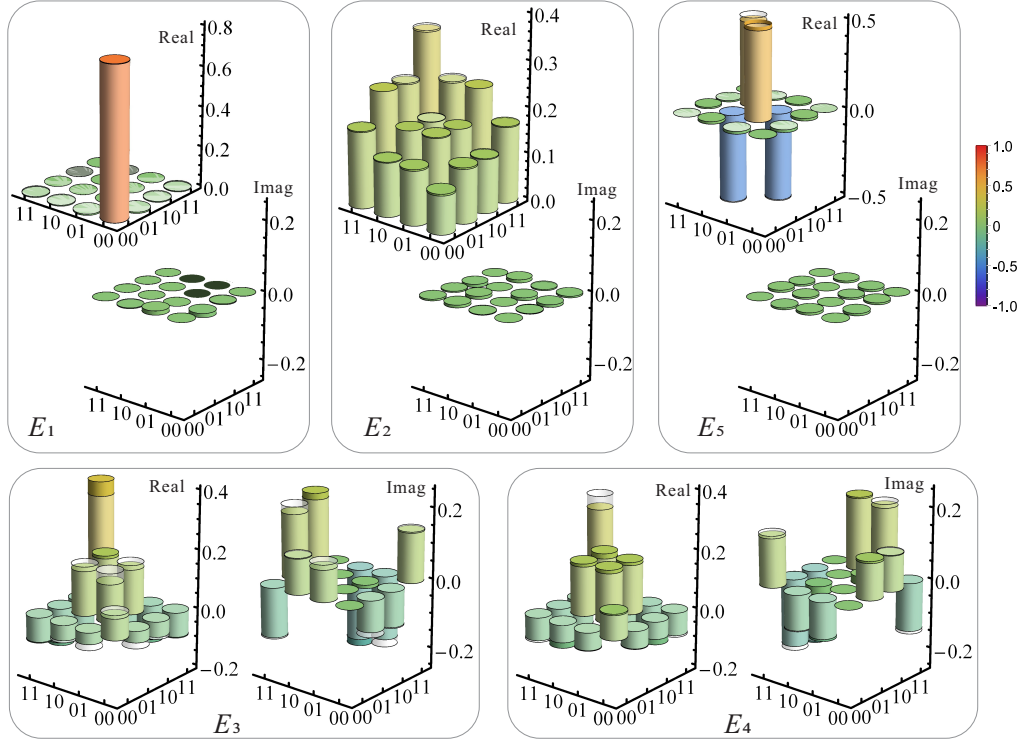


FIG. S2: Results on measurement tomography of the collective SIC-POVM realized in the experiment. The matrix elements of the real (Real) and imaginary (Imag) parts of the five POVM elements E_1 to E_5 are plotted using solid colours. For comparison, the counterparts of the ideal POVM are plotted as wire frames.

IV. SCALING OF THE MEAN INFIDELITY WITH THE SAMPLE SIZE

In this supplement, we provide additional details on the scaling of the mean infidelity with the sample size in quantum state tomography with the collective SIC-POVM. To complement the results presented in the main text, we first illustrate the scaling of the mean infidelity $1 - F$ achieved by the collective SIC-POVM for mixed states. We then present the scaling exponents for both pure states and mixed states.

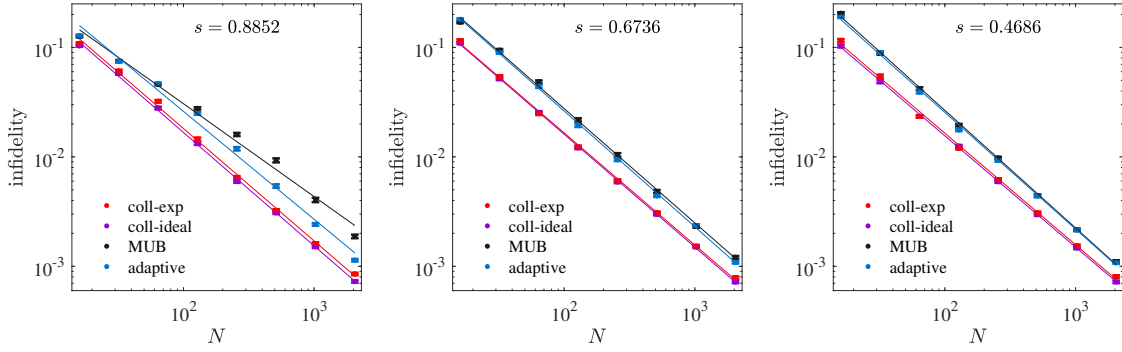


FIG. S3: Scaling of the mean infidelity in the tomography of mixed states with the collective SIC-POVM (both experiment and simulation). The performances of MUB and two-step adaptive measurements (simulation) are shown for comparison. The three plots correspond to the tomography of three mixed states whose Bloch vectors align with the same direction $\hat{s} = (0.490, -0.631, 0.602)$ and have lengths $s = 0.885, 0.674$ and 0.469 , respectively. Here N is the sample size, ranging from 16 to 2048. Each data point is the average of 1000 repetitions, and the error bar denotes the standard deviation.

A. Scaling of the mean infidelity for mixed states

Three mixed states were considered; their Bloch vectors align with the same randomly-chosen direction $\hat{s} = (0.490, -0.631, 0.602)$, with lengths $s = 0.885, 0.674$ and 0.469 , respectively. The experimental result as well as the simulation result on the ideal collective SIC-POVM are shown in Fig. S3. Also shown as benchmarks are the simulation results on the performances of two popular alternative schemes based on mutually unbiased bases (MUB) for a qubit [41–44]. Similar to the case of pure states, the efficiency of the collective SIC-POVM is almost independent of the input state; the infidelity approximately scales as $O(1/N)$ for all states investigated.

By contrast, the scaling behavior for MUB is sensitive to the purity of the input state. When the input mixed state has a high purity (see the left plot in Fig. S3), the infidelity scales as $O(1/\sqrt{N})$ when N is small, while it scales as $O(1/N)$ when N is large. The transition region depends on the purity of the input state. In the special case of a pure state ($s = 1$), the $O(1/\sqrt{N})$ scaling approximately holds for all N (see the middle and right plots in Fig. 4). When the state is highly mixed, MUB achieves almost the same scaling $O(1/N)$ as the collective SIC-POVM, but the infidelity is still larger by a constant factor of about 1.5 (see the right plot in Fig. S3).

B. Scaling exponents

In the main text, we investigated the scaling of the mean infidelity $1 - F$ achieved by the collective SIC-POVM with the sample size N . Three pure states with Bloch vectors $(0, 0, 1)$, $\frac{1}{\sqrt{2}}(1, 0, 1)$ and $\frac{1}{\sqrt{3}}(1, 1, 1)$ were considered. The experimental result as well as the simulation result on the ideal collective SIC-POVM are shown in Fig. 4 in the main text. Also shown as benchmarks are the simulation results on the performances of two popular alternative schemes: one based on mutually unbiased bases (MUB) for a qubit [41–44] and the other based on two-step adaptive measurements proposed in Ref. [45] (cf. Refs. [40, 46, 47]). In addition, three mixed states were investigated in Sec. IV A in this supplement; see Fig. S3.

To quantify the distinction between different measurement schemes, experimental data and numerical data are fitted to power laws of the form $1 - F = \beta N^{-p}$. The exponents p are shown in Table S2. According to this table, the efficiency of the collective SIC-POVM is almost independent of the input state; the infidelity approximately scales as $O(1/N)$ for all states investigated. By contrast, the scaling behavior for MUB is very sensitive to the input state. For states with high purities, the scaling is usually much worse except when the input state aligns with one of the POVM elements, which corresponds to “known state tomography” [45].

TABLE S2: Scaling exponents of the mean infidelity $1 - F$ against the sample size N in quantum state tomography. The performance of the collective SIC-POVM (both experiment and simulation) is compared with that of MUB and local adaptive measurements (simulation). The first three columns represent the results on three pure states with Bloch vectors as specified, while the last three columns represent results on three mixed states whose Bloch vectors align with the same direction $\hat{s} = (0.490, -0.631, 0.602)$, with lengths s as specified. The data presented in Figs. 4 and S3 are fitted to the formula $1 - F = \beta N^{-p}$. The scaling exponents p for the above six states and four measurement schemes are shown in this table. The values inside the parentheses represent the uncertainties in the last two digits of the best-fitted values within 95% confidence intervals.

States	$(0, 0, 1)$	$\frac{1}{\sqrt{2}}(1, 0, 1)$	$\frac{1}{\sqrt{3}}(1, 1, 1)$	$s = 0.885$	$s = 0.674$	$s = 0.469$
coll-exp	1.047(53)	1.002(09)	1.004(12)	1.028(40)	1.025(25)	1.019(37)
coll-ideal	0.999(20)	0.977(20)	1.004(16)	1.036(28)	1.031(14)	1.016(15)
MUB	1.008(11)	0.583(29)	0.571(29)	0.849(86)	1.045(36)	1.074(27)
adaptive	0.970(28)	0.850(54)	0.873(57)	0.986(90)	1.058(25)	1.066(33)

V. IMPLEMENTATION OF THE MAXIMUM LIKELIHOOD ESTIMATION

Consider quantum state tomography with a POVM $\{E_j\}_{j=1}^K$ composed of K outcomes. If the quantum system is characterized by the state ϱ , then the probability of obtaining outcome j is $p_j = \text{tr}(\varrho E_j)$. Suppose the POVM is performed N times on N identically prepared quantum systems, and outcome j occurs n_j times with $\sum_j n_j = N$. Now our task is to infer the state of the quantum system from the measurement data $D = \{n_1, n_2, \dots, n_K\}$.

As a popular estimation strategy in quantum tomography, the ML estimation [4] searches for the quantum state $\hat{\varrho}_{\text{ML}}$ that maximizes the likelihood function, i.e.,

$$\hat{\varrho}_{\text{ML}} := \arg \max_{\varrho} L(D|\varrho), \quad \text{with } L(D|\varrho) = \prod_j p_j^{n_j}. \quad (\text{S12})$$

In practice, it is more convenient to work with the normalized log-likelihood function defined as $\mathcal{F}(\varrho) := \frac{1}{N} \ln L(D|\varrho)$. In quantum state tomography with individual measurements, the function $\mathcal{F}(\varrho)$ is concave in ϱ and thus has a unique maximum in the quantum state space, which is convex. In addition, iterative algorithms can be employed by following the gradient

$$G(\varrho) = \sum_j \frac{f_j}{p_j} E_j \quad (\text{S13})$$

of $\mathcal{F}(\varrho)$, where $f_j = n_j/N$ is the relative frequency. In quantum state tomography with two-copy collective measurements as considered in this work, however, two-copy quantum states comprise only a subset of the two-qubit state space. Therefore, standard ML algorithms do not apply directly.

Recently, a new optimization strategy, i.e., the accelerated projected-gradient (APG) method was introduced in quantum tomography [49], using which all constraints can be cast into a projection operation. In the current scenario, we have to make sure that the update for ϱ at each iterative step takes on the form $\varrho = \rho^{\otimes 2}$. To this end, we introduce the projection operation \mathcal{P} as follows,

$$\tilde{\varrho} = \mathcal{P}(\varrho) : \tilde{\varrho} = \tilde{\rho}^{\otimes 2} \text{ with } \tilde{\rho} := \arg \min_{\rho} \|\varrho - \rho^{\otimes 2}\|_{\text{HS}}, \quad (\text{S14})$$

where $\|\cdot\|_{\text{HS}}$ denotes the Hilbert-Schmidt norm. This optimization can be done easily by properly parametrizing single-qubit states. Then, we modify the APG algorithm presented in Ref. [49] as follows:

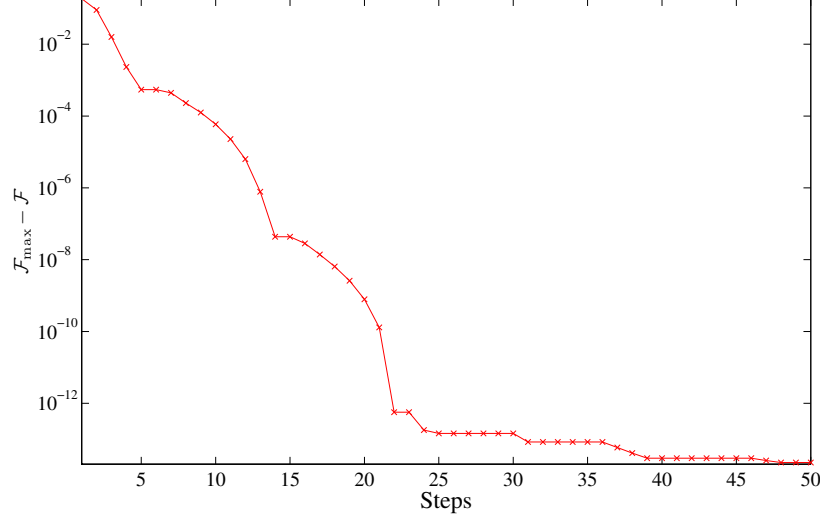


FIG. S4: Convergence of the APG algorithm in quantum state tomography with the collective SIC-POVM. The vertical axis represents the deviation $\mathcal{F}_{\max} - \mathcal{F}$ of the normalized log-likelihood \mathcal{F} at each iterative step from the maximum value \mathcal{F}_{\max} . In the numerical simulation, the frequencies of obtaining the five outcomes are set to the corresponding probabilities when the collective SIC-POVM is performed on a two-copy state. The APG algorithm is run until the machine precision is reached. The figure shows that the algorithm converges very quickly.

Algorithm: APG for collective measurements

Given $\epsilon > 0$ and $0 < \beta < 1$.

Initialize with any state $\varrho_0 = \rho_0^{\otimes 2}$, $\mathcal{F}_0 = \mathcal{F}(\varrho_0)$; set $\tau_0 = \varrho_0$, $\theta_0 = 1$.

for $k = 1, 2, \dots$, **do**

 Update $\varrho_k = \mathcal{P}[\tau_{k-1} + \epsilon G(\tau_{k-1})]$ according to Eq. (S14), $\mathcal{F}_k = \mathcal{F}(\varrho_k)$.

 Termination criterion!

if $\mathcal{F}_k < \mathcal{F}_{k-1}$ **then** (Restart)

 Reset $\epsilon = \beta\epsilon$, $\varrho_k = \varrho_{k-1}$, $\tau_k = \varrho_k$, and $\theta_k = 1$.

else (Accelerate)

 Set $\theta_k = \frac{1}{2} \left(1 + \sqrt{1 + 4\theta_{k-1}^2} \right)$, then update $\tau_k = \varrho_k + \frac{\theta_{k-1}-1}{\theta_k} (\varrho_k - \varrho_{k-1})$.

end if

end for

Generally speaking, the APG algorithm works in a similar way to those conventional gradient approaches, but with a tweaked gradient direction in each step to boost the convergence. Specifically, each update of the target ϱ in APG is based on another state τ , which gives each update some “momentum” from the previous step. The momentum is controlled by the parameter θ , which is reset to 1 whenever it causes the current step to point too far from the direction specified by $G(\cdot)$. Upon convergence, ϱ and τ will eventually merge to the same point. For more technical details about the APG algorithm, e.g., the ‘Restart’ and ‘Accelerate’ operations, see Ref. [49] and references therein.

Figure S4 illustrates the convergence of the APG algorithm applied to the collective SIC-POVM. In the numerical simulation, a qubit state ρ is generated randomly, and the frequency of obtaining each outcome is set to the corresponding probability, that is, $f_j = p_j = \text{tr}(\rho^{\otimes 2} E_j)$, where E_j for $j = 1$ to 5 are the five outcomes of the collective SIC-POVM. In this example, the maximum value \mathcal{F}_{\max} of the normalized log-likelihood function is attained at the true state ρ ; the deviation $\mathcal{F}_{\max} - \mathcal{F}$ from the maximum value is plotted as a function of the number of steps. The figure shows that the APG algorithm converges very quickly.